



1 **FATE OF DISSOLVED ORGANIC MATTER ACROSS THE PERMAFROST-NEARSHORE WATER**

2 **CONTINUUM : ROLE OF THE INTERTIDAL SEDIMENTS**

3 Aude Flamand¹ (ORCID : 0000-0001-9983-4176)

4 Jean-François Lapierre^{2,3} (ORCID : 0000-0001-5862-7955)

5 Gwénaëlle Chaillou¹ (ORCID: 0000-0002-4170-8852)

6 ¹ Québec-Océan, Institut des Sciences de la Mer de Rimouski, Université du Québec à Rimouski, 310 Allée des

7 Ursulines, Rimouski, Québec, Canada, G5L 3A1.

8 ² Département de sciences biologiques, Université de Montréal, 1375 Avenue Thérèse-Lavoie-Roux, Montréal,

9 Québec, Canada, H2V 0B3.

10 ³ Groupe de Recherche Interuniversitaire en Limnologie (GRIL).

11 **Corresponding Author:** Gwénaëlle Chaillou. Email: gwenaelle_chaillou@uqar.ca

12



13 **ABSTRACT**

14 Increasing rates of coastal erosion and permafrost thaw along the Arctic coastline represent a major lateral
15 source of dissolved organic matter (DOM) to the coastal environment, where it can meet multiple fates
16 depending on its origin and composition. Along the (ground)water flow path, Iron (Fe)-hydroxides play an
17 important role in the retention of terrestrial organic matter, but its role on DOM released from coastal thawing
18 permafrost specifically remains poorly understood. To address this gap, we sampled permafrost meltwater,
19 beach groundwater, and seawater samples from several coastal bluffs transects up to 2 km from the shoreline.
20 Across the salinity gradient – from permafrost meltwater to nearshore waters - we found that dissolved organic
21 carbon (DOC) and chromophoric dissolved organic matter (CDOM) concentrations decreased drastically,
22 indicating significant removal processes along this continuum. Optical indices ($a_{CDOM350}$, $SUVA_{254}$, HIX)
23 reflected changes in DOM composition and aromaticity, suggesting microbial degradation and mineral-organic
24 interactions occur to transform DOM. Furthermore, a PARAFAC analysis of fluorescent DOM indicated that
25 permafrost-derived DOM had a high molecular weight (HMW), humic, and terrigenous origin, while coastal
26 ocean-derived FDOM was protein-rich, low molecular weight (LMW), and from microbial (autochthonous)
27 origin. The optical signature of permafrost meltwater faded along the permafrost-nearshore water continuum.
28 Controlled experiments with excess Fe^{2+} along constant oxygen bubbling showed a rapid (within 6 hours) and
29 major decrease in DOC and CDOM, suggesting interaction with reactive Fe-hydroxides, acting as a permanent
30 or temporary trap of permafrost-derived DOM. Overall, our findings highlight the role of intertidal and
31 nearshore zones where subsurface flows regulate the persistence and reactivity of terrestrial DOM as it transits
32 from permafrost to marine environments in the Arctic.

33 **KEYWORDS:** permafrost, Arctic coastal ocean, dissolved organic matter, dissolved organic carbon, iron
34 hydroxide.

35

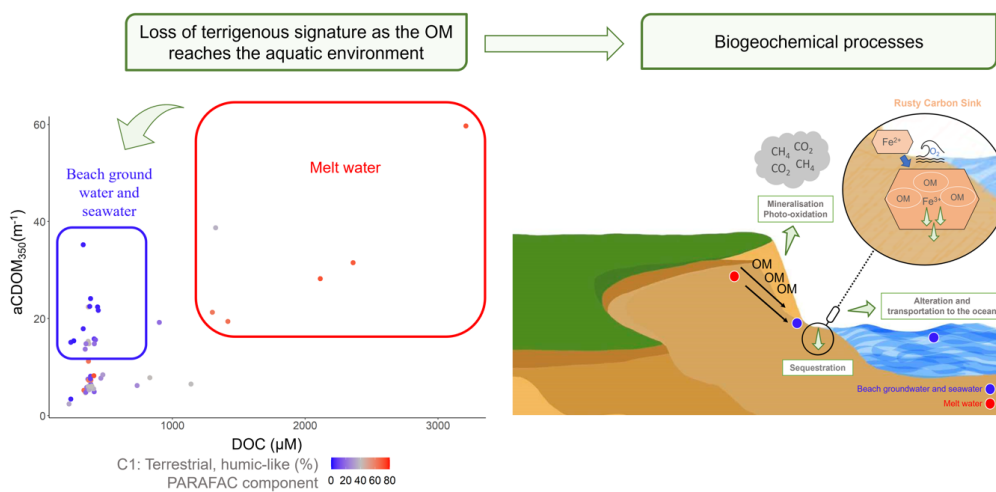
36



37

38 **GRAPHICAL ABSTRACT**

39



40



41 **1 INTRODUCTION**

42 Permafrost stores around 1,300 Pg of organic carbon (OC) within its 13.9×10^6 km² surface area, which
43 represents 60 % of the world's carbon stored in 15 % of the world's soil (Obu et al. 2019; Schuur et al. 2015).
44 The Arctic permafrost coastline is greatly impacted by global changes inducing unprecedented thawing rates,
45 along with the deepening of the active layer, which, in turn, increases subsurface transport (Jones et al. 2020;
46 Lantuit et al. 2012). Unlithified and ice-bonded permafrost cliffs, such as those that span the Beaufort Sea, are
47 susceptible to coastal erosion. Over the past twenty years, they have experienced one of the highest coastal
48 erosion rates recorded in the Arctic, with a recorded rate of 1.1 m yr⁻¹ between 1950 and 2000. This rate has
49 increased by 80–160 % in the last two decades (Jones et al. 2020; Lantuit et al. 2012). Accelerating coastline
50 erosion is supplying increasing quantities of terrestrial materials (Kipp et al. 2018), associated nutrients (Fritz
51 et al. 2017), carbon (Bristol et al. 2021), and contaminants (Kwasigroch et al. 2018) to the nearshore and coastal
52 ocean. This additional, non-point source of solutes is remobilized in late summer mostly when thaw depths are
53 at a maximum, and rapidly reaches nearshore waters via surficial and subsurface flows (Walvoord & Striegl
54 2007; Lecher, 2017).

55 Dissolved organic matter (DOM) represents a fundamental link between terrestrial and aquatic carbon cycles
56 and plays a significant role in the biogeochemistry of aquatic ecosystems (Hedges & Keil 1995). Terrestrially
57 derived dissolved organic matter (tDOM) strongly influences coastal ecosystem functioning (Vonk et al. 2015),
58 food web dynamics (McMeans et al. 2015; Thingstad et al. 2008), ocean chemistry (Guo et al. 2007; Stedmon
59 et al. 2011; Vonk et al. 2014) and optical conditions (Fichot et al. 2013; Matsuoka et al. 2012). A fraction of
60 this tDOM can be rapidly mineralized through microbial and photochemical processes, affecting nutrient
61 budgets, air-sea CO₂ exchanges, biological productivity, as well as acidification, in coastal waters (Kaiser et al.
62 2017a; Kaiser et al. 2017b). For example, Kaiser et al. (2017a) showed that ~50 % of the annual tDOC
63 discharged by Siberian rivers was mineralized along the land-sea continuum: tDOC is strongly removed and
64 lost as CO₂ along the transport. Therefore, only a small fraction potentially persists in the ocean over centuries
65 and millennia (Fichot & Benner 2014; Kaiser et al. 2017a). While the export of tDOC is known to strongly



66 influence the arctic marine ecosystem, little is known about the role and importance of erosional and thawing
67 inputs in shaping the ecology and chemistry of nearshore coastal waters. This is due not only to the stochastic
68 nature of erosion and thaw-related inputs but also to the complex nature of mineral and organic phases and their
69 role in tDOM stabilization along the flow path. The mechanisms and processes related to organic matter
70 transformations occurring at mineral-organic interfaces are complex (see Li et al., 2023; and references therein),
71 particularly in dynamic systems where biological, geochemical, and redox conditions interplay to influence the
72 concentrations and molecular compositions of DOM. For example, the formation of an iron (Fe) curtain can
73 represent an important mechanism of terrigenous OC storage (Zhou et al. 2024), particularly along subterranean
74 estuaries (STE) and intertidal discharge zones (Riedel et al., 2013; Linkhorst et al., 2017; Sirois et al. 2018;
75 Zhou et al., 2023). In temperate and subarctic regions, STE is a complex hydrogeochemical system along the
76 groundwater flow path which acts as a biogeochemical reactor where DOM is mineralized and/or trapped
77 (Anschutz et al., 2009; Sirois et al., 2018; Hébert et al., 2022). Its role as a transient or permanent terrestrial
78 organic carbon sink in the Arctic region is not known but could be a key zone of permafrost-derived DOM
79 trapping. The behaviour and optical properties of the permafrost-derived DOM as it reaches STE and nearshore
80 waters remain unclear, as does their affinity with amorphous Fe-hydroxide in STE.

81 To understand the behaviour of DOM along the land-sea continuum, absorbance- and fluorescence-derived
82 indices are commonly used to characterize its origin, reactivity, and transformations (Fichot & Benner 2014;
83 Meilleur et al. 2023; Stedmon et al. 2003). In addition, the use of excitation-emission matrices (EEM) with
84 parallel factor analysis (EEM-PARAFAC) of FDOM (Bro 1997) can allow for assessment of the composition
85 and sources of permafrost-derived DOM delivered to nearshore waters via surface runoff and groundwaters.
86 Recent findings by Fouché et al., (2020) characterized the permafrost-derived DOM as low molecular weight
87 (LMW), proteinaceous and with low aromaticity, with this signature fading rapidly during lateral flow
88 downslope of the permafrost table and within the fluvial continuum. This suggests that permafrost-derived
89 DOM may be rapidly lost in the permafrost – nearshore water continuum. However, further investigation is
90 needed to understand the mechanisms and processes that control this loss as DOM flows within intertidal
91 sediments and into the coastal Arctic Ocean. This study aims to characterize the transformation pathways of



92 DOM released from the thawing of coastal permafrost cliffs, while better understanding the role of beach
93 groundwater in the transfer of tDOM from permafrost to nearshore waters. More specifically, we have
94 developed a site-specific scale approach (<2 km) in the Kugmallit Bay (NWT, Canada) to optically characterize
95 and follow the behaviour of the DOC and DOM (CDOM and FDOM) along the permafrost – nearshore water
96 continuum. In addition, the affinity of permafrost-derived DOM and DOC with amorphous Fe-hydroxides, as
97 they flow from the subsurface to nearshore waters, was experimentally tested.

98 **2 MATERIALS AND METHODS**

99 ***2.1 Site Description***

100 The study area is located in the Inuvialuit Settlement Region of the Northwest Territories adjacent to the
101 Mackenzie Delta region, the 4th largest river draining in the Arctic Ocean (Macdonald et al. 1998). A first
102 sampling campaign took place from July 24th to August 6th, 2019, and a second campaign from June 22nd to
103 August 31st, 2021, when thaw rates were at a maximum. About 60 samples were collected at four sampling sites
104 characterized by continuous permafrost coastal cliffs with thaw slumps surrounded by sandy and clay beaches:
105 Tuktoyaktuk Island, Peninsula Point, Crumbling Point and Reindeer Island (Fig. 1). Tuktoyaktuk Island, the
106 main sampling site (N=27), is characterized by a coastal bluff of approximately 9 m high, 1.5 km length and
107 100 m width (Ouellette 2021) and is located across the Hamlet of Tuktoyaktuk, in the south-east of the
108 Kugmallit Bay. The island loses ~1.8 m of shore per year due to erosion induced by storms and thawing
109 permafrost; an increase of 22% has been observed in the last 15 years (Berry et al. 2021; Tanguy et al. 2023;
110 Whalen et al. 2022), and the site is projected to entirely disappear within 20–30 years (Jones et al. 2020). In
111 front of the cliffs, a ~50 m wide beach is composed of a 0.3 to 0.5 m deep layer of fine to medium sandy
112 sediment that overlays a frozen clay horizon. Peninsula Point site is in the Pingo Canadian Landmark, southwest
113 of Tuktoyaktuk Island, and forms a complex retrogressive thaw slump system known for the presence of a
114 massive ice body of between 5 m and 20 m thickness (Mackay, 1986). Large muddy lobes composed of thawed
115 permafrost material and meltwater flow downslope to the nearshore (Hayes et al., 2022) where they sporadically



116 cover sandy intertidal sediment. Based on Hayes (2020), the recent shoreline retreat was of ~ 3.4 m yr⁻¹ from
117 1985 to 2018. Crumbling Point is also a retrogressive thaw slump system, located at the extreme northwest of
118 the Kugmallit Bay. Finally, Reindeer Island is located at the north of Richards Island, in an important lagoon
119 system formed by thermokarst lakes surrounded by coastal bluffs. To the best of our knowledge, there are no
120 published data on the coastal retreat in these zones, but it could be similar, at least, to what is reported in the
121 Canadian Beaufort-sea region (~ 0.5 m a⁻¹ (Solomon, 2005)) and likely reach very high local retreat rates as
122 presently observed in some location, as in Pullen Island (>12 m a⁻¹ (Berry et al. 2021)).

123 *2.2 Water and Sediment Sampling*

124 At each site, we carried out a site-specific scale sampling where different water sample types were collected
125 along a transect, from the coastal permafrost cliffs, through the sandy intertidal zones, to the near-shore
126 seawater. Meltwater and groundwater (here defined as porewater into fine sandy coastal sediment) samples
127 were collected on coastal permafrost slumps and the adjacent sandy shore, respectively. In contrast, seawater
128 samples were collected in front of each study site between 0.5 to 1 km from the coastline. Meltwater was directly
129 sampled in puddles formed on the slope of thaw slumps using a submersible pump. For beach groundwater,
130 push-point piezometers were inserted to ~ 50 cm depth into the sandy ground, above the frozen clay layer, in
131 front of thaw slumps in the intertidal zone and water was continuously pumped by a Solinst® peristaltic pump.
132 A massive ice sample was also collected from a permafrost core collected at Richard Island. The core was
133 sectionized and the different sections were defrosted gently in a hermetically closed acid-cleaned bucket. The
134 thawing water was collected by a peristaltic pump. Finally, seawater was collected in front of the slump systems
135 using a submersible pump placed between 0.5 and 1 m depth below the surface from a small vessel. For each
136 location, water samples were pumped into an online flow cell where practical salinity (S_p), temperature and
137 oxygen saturation were monitored using a daily calibrated multiparametric probe (600QS, YSI Inc.).

138 After these parameters stabilized, water samples were collected for CDOM/FDOM into acid-washed 60 mL
139 glass amber bottles after on-line filtration through a 0.22 μ m Millipore Opticap® XL4 cartridge with a
140 Durapore® membrane. The samples were stored in the dark at 4 °C. Total dissolved Fe samples were collected



141 in 60 mL metal-free Falcon® tubes after filtration through the same 0.22 µm Millipore Opticap cartridge. The
142 samples were acidified with 3 drops of 70 % nitric acid to prevent the re-oxidation of reduced trace metals and
143 stored at 4 °C. DOC samples were taken using 60 mL acid-cleaned polypropylene syringes and rapidly filtered
144 with pre-combusted (450 °C for 5–6 hours) 0.7 µm glass microfiber filters GF/F Whatman™ and stored in pre-
145 combusted and acid-washed 12 mL borosilicate EPA tubes with PTFE caps. The DOC samples were acidified
146 to pH <2 with high purity HCl 2N and stored in the dark at 4 °C until analysis. During the 2019 campaign,
147 samples were also collected in 30 ml scintillation vials, hermetically sealed for further water isotope analysis.

148 *2.3 Chemical and Optical Analysis*

149 Stable isotopes of water were analyzed by EA-IRMS during the following year after the collection. Accuracies
150 are ±0.05 ‰ and ±1 ‰ for δ¹⁸O and δ²H, respectively. Reference materials were used throughout the isotopic
151 water analyses and isotopic analyses are reported compared to the international Vienna Standard Mean Ocean
152 Water (VSMOW). DOC samples were analyzed a few weeks after data collection by Total Organic Carbon
153 analyzer (TOC-Vcpn Shimadzu) based on the method of Wurl and Tsai (2009). The analytical uncertainty was
154 less than 4 %, while the detection limit was 5.8 µM. To ensure instrument stability, fresh acidified deionized
155 water (blank) and a standard solution (86.6 ± 1.7 µM) were regularly analyzed. The concentration of total
156 dissolved iron (Fe_{tot}) was measured according to the ferrozine method proposed by Stookey (1970) and adapted
157 by Viollier et al. (2000). The detection limit of the method was 0.4 µM and the reproducibility was better than
158 0.3 %.

159 Absorbance and fluorescence spectroscopy were used for the measurement of the chromophoric and fluorescent
160 fractions of DOM (CDOM and FDOM) a few weeks after sampling. The CDOM absorbance was measured
161 using a Lambda 850 UV-VIS Perkin Elmer spectrophotometer with 1 cm path-length quartz cuvettes.
162 Measurements were taken from 220 to 800 nm at 1 nm intervals with a scanning speed of 100 nm min⁻¹ and a
163 5 nm slit width. Blanks and references were measured using fresh Milli-Q water. The FDOM was measured
164 concomitantly using a Varian Cary Eclipse spectrofluorometer. Fluorescence spectra were measured within the
165 emission wavelengths of 220 to 600 nm and the excitation wavelengths of 220 to 450 nm at 5 nm intervals as



166 described by Couturier et al. (2016). Similarly, fresh Milli-Q water was used as a blank to rinse the cuvette in
167 between samples. Fresh deionized water was used as a blank and absorbance measurements of the samples were
168 used to correct the inner-filter effect and the dataset was corrected for Rayleigh and Raman scattering, according
169 to the method used by Pucher et al. (2019).

170 *2.4 Optical-derived indices and PARAFAC model*

171 Absorbance and fluorescence indices were extracted using the staRdom toolbox on the R Studio Software
172 (Pucher et al. 2019). Different indices were explored but here we only reported 3 of them to characterize the
173 DOM pool because they presented significantly different values between the different categories of samples
174 (e.i. groundwater, melting water, massive ice, and seawater). The spectral absorption coefficient at 350 nm
175 ($a_{CDOM350}$) was used as a tracer of CDOM absorption and content. It was calculated as 2.303 times the
176 absorbance at the wavelength $\lambda=350$ nm divided by the pathlength of the cuvette (m). The specific UV
177 absorbance ($SUVA_{254}$ in $mgC L^{-1}$) was calculated as the absorbance at the wavelength $\lambda=254$ nm divided by
178 the DOC concentration. It allows tracking the CDOM aromaticity (Weishaar et al. 2003): greater $SUVA_{254}$
179 values correspond to a greater degree of aromaticity (Helms et al. 2008). It also has been shown as positively
180 correlated with the molecular weight of the DOM compounds. In the FDOM pool, the humification index
181 (HIX) corresponds to the peak area under emission of 435–480 nm divided by the peak area under emission of
182 300–345 nm, at an excitation of 254 nm. HIX is an indicator of humic substances and the extent of humification
183 of DOM compounds (Hansen et al., 2016; Ohno, 2002): higher HIX indicates a greater humification of the
184 DOM source and HMW compounds.

185 In combination with the absorbance and fluorescence indices, a PARAFAC model was developed to investigate
186 further the composition and the sources of FDOM across samples (Bro 1997; Murphy et al. 2013; Stedmon et
187 al. 2003). Three components were validated using the method adapted from Pucher et al. (2019), in R studio
188 ($R^2 > 92\%$). The components were also matched with the literature for identification and external validation,
189 using OpenFluor (Murphy et al. 2013). The three fluorescing peaks (C1-3) identified are presented in Fig. 2 and
190 their theoretical characteristics based on the literature are summarized in Table 1. Briefly, C1 and C3



191 components are mainly related to terrestrial and humic-like compounds of high (HMW) and low molecular
192 weight (LWM), respectively. In contrast, the C2 component is likely related to freshly produced protein-like
193 compounds, of autochthonous origin and is mainly composed of LMW compounds.

194 *2.5 Affinity of Permafrost derived DOM with Iron Hydroxides*

195 Iron-spiked experiments were performed to assess the affinity of flowing DOM and DOC with amorphous Fe-
196 hydroxides. Samples of beach groundwater, seawater and meltwater were collected in 1-L acid-washed glass
197 bottles. In the laboratory, ~20 mM of FeCl₂·4H₂O were added to filtered (Pall® GWV High-Capacity
198 Groundwater Sampling Capsule, 0.45 µm porosity) water samples. The concentration of Fe was intentionally
199 added in excess compared to Fe_{tot} concentration measured in the samples (median Fe_{tot} concentration ~ 1.1 µmol
200 L⁻¹; with maximum values of 680 µmol L⁻¹) to favor the oxidative precipitation of amorphous Fe-hydroxides.
201 The experiments were performed rapidly after the sampling (<24h) during the 2021 campaign. The
202 experimental bottles were kept in the dark, at room temperature (~ 21°C). They were continuously air-bubbled
203 to maintain well-oxygenated conditions and favoured the precipitation of Fe-hydroxides. Sub-samples for DOC
204 and CDOM analysis were collected at times 0, 6, 12, 24 and 48 hours. DOC and CDOM samples were analyzed
205 as previously described.

206 **3 RESULTS AND DISCUSSION**

207 *3.1 Physico-chemical characteristics along the permafrost-nearshore continuum*

208 In this study, we refer to samples collected at the nearshore as “seawater”; nevertheless, we acknowledge that
209 these samples more accurately represent a brackish environment, with practical salinity *Sp* values ranging from
210 0.5 to 20. The massive ice and meltwater samples exhibited the lowest salinities with *Sp*<1 whereas the salinity
211 of beach groundwater samples ranged between 0 and 5.4. The *Sp* range measured in these groundwater samples
212 mostly reflected the tidal pumping effect and the recirculation of the seawater within the permeable sediments.
213 The higher salinities (*Sp*>5.4) were only measured in seawater samples. The temperature varied between 8.1
214 and 16.7 °C (with a mean value of 13.0 ± 2.6 °C) with the higher temperatures measured in meltwater and some



215 beach groundwater samples. Oxygen saturations ranged from 6 to 141 % of saturation. The nearshore surface
216 seawater and the meltwater samples were all over-saturated because of their contact with the atmosphere.
217 However, the low-salinity beach groundwater samples exhibited low oxygen saturation (6 - 48 %) despite the
218 recirculation of well-oxygenated seawater. Redox oscillations and transitory oxygen-depleted conditions are
219 observed in microtidal sandy intertidal zones (Hébert et al. 2022; Sirois et al. 2018; Waska et al. 2021) where
220 the tidally input of oxygen is rapidly consumed by heterotrophic processes (Chaillou et al., 2024; Moore et al.,
221 2024).

222 ***3.2 Origin of the subsurface water flow in the intertidal zone***

223 The $\delta^{18}\text{O}$ and $\delta^2\text{H}$ values measured in water samples collected in 2019, mostly at Tuktoyaktuk Island, Peninsula
224 Point sites, and Crumbling Point (Fig. 1), ranged from -28 to -10 ‰ and from -215 to -82 ‰, respectively, the
225 massive ice sample (N=1) presenting the most depleted signature (Fig. 3). These depleted values are largely
226 explained by low air temperatures and are typical of permafrost hydrology reported in the western Arctic (Fritz
227 et al. 2011; Utting et al., 2012). The samples are well aligned along the local meteoric water line (LMWL; $\delta^2\text{H}$
228 = $7.39 \times \delta^{18}\text{O} - 6.70$; Fritz et al., 2022), whatever their salinity values, except for the three (3) meltwater samples
229 that are slightly below it, probably due to evaporation processes at the surface. The similarity between the
230 massive ice, beach groundwater and seawater isotopic distribution and the LMWL regression line suggests a
231 common meteoric origin, probably from permafrost watershed. The subsurface flow that transits across the
232 beach sediment does not seem to be affected by surficial processes (e.g. evaporation process), as observed in
233 the meltwaters, likely limiting photochemical degradation of the flowing DOM. These results agree with recent
234 study of Kipp et al. (submitted) that showed the occurrence of high activities of radon isotope (^{222}Rn) in the
235 same groundwater samples, a noble gas that rapidly escapes as soon as it is in contact with the atmosphere. The
236 absence of light and the low oxygen content in the subsurface were then suitable for microbial transformations
237 and mineral-organic interactions as observed in other STEs, both limiting the export of tDOM into adjacent
238 coastal waters (Couturier et al., 2017; Linkhorst et al., 2017; Sirois et al. 2018; Hébert et al., 2022; Zhou et al.,
239 2023).



240 *3.3 Behaviour of the DOC and DOM pool*

241 The distribution of the variables used to characterize the DOM pool along the permafrost-nearshore water
242 continuum is presented in Fig. 4. The DOC concentrations dropped from 2,360 $\mu\text{mol L}^{-1}$ in meltwater samples
243 to 236 $\mu\text{mol L}^{-1}$ in the saltiest seawater sample (Fig. 4A). The concentrations decreased sharply along the
244 continuum to reach values lower than 400 $\mu\text{mol L}^{-1}$ in beach groundwater and seawater, whatever the salinity.
245 Absorption coefficients at 350 nm were less variable, from 2 to an extreme value of 134 m^{-1} measured in one
246 meltwater sample (Fig. 4B). As for the DOC concentrations, the aCDOM₃₅₀ decreased along the continuum,
247 with a median value of 24.0 m^{-1} in meltwater samples and median values of 8.4 and 7.8 m^{-1} in beach groundwater
248 and seawater, respectively. The HIX values exhibited a large range of values for each type of sample. The
249 median values, however, tended to decrease along the continuum, from 3.5 (unitless) in meltwater samples to
250 1.4 in beach groundwater and 0.8 in seawater samples (Fig. 4C). Whereas DOC, aCDOM₃₅₀ and HIX values
251 negatively decreased along the continuum, the SUVA₂₅₄ values tend to increase from the massive ice and
252 meltwater samples to the beach groundwater and nearshore seawater samples. The median SUVA₂₅₄ value of
253 2.4 mg C L^{-1} in the meltwater samples increased slightly to median values of 2.9 mg C L^{-1} in the beach
254 groundwater samples and they reached a median value of 3.4 mg C L^{-1} in seawater samples (Fig. 4D).

255 DOC concentration and aCDOM are routinely used as proxies to characterize the quantity and quality of the
256 DOM pool in aquatic continuum. The relationships in between is used to reveal the biogeochemical source and
257 processing of organic matter through physical and biogeochemical conditions (Massicotte et al., 2017; Fichot
258 and Benner, 2011; Spencer et al., 2013; Stedmon et al., 2003). A linear relationship between DOC and aCDOM
259 means that the DOC portion stays constant within the DOM pool, whatever the salinity and their respective
260 origin. In freshwater systems, for example, DOC concentrations were often highly correlated with the DOM
261 pool (Frenette et al., 2012; Massicotte et al., 2017 and reference therein). However, the decoupling between
262 DOC and aCDOM₃₅₀ was observed as soon as mixing, photo-oxidation, and microbial degradation operate at
263 different rates on DOC and CDOM/FDOM fractions of the DOM pool (Del Vecchio and Blough, 2004; Nelson
264 et al., 1998; Nelson and Siegel, 2013). This decoupling suggests active processing of DOM during its transit
265 from freshwater to marine environment, for example, in subterranean estuaries in which the photo-oxidation



266 processes were null, the CDOM and DOC coupling resulted from microbial degradation that simultaneously
267 mineralized both (Hébert et al., 2022). In contrast, Couturier et al. (2016) showed a strong CDOM-DOC
268 decoupling in another STE, with most of the high molecular weight (HMW) DOM compounds tending to be
269 trapped in the system and not reaching the receiving nearshore waters. In this latter STE, Sirois et al. (2018)
270 highlighted the importance of the Fe curtain, where reactive Fe phases in sediments act as an efficient trap for
271 terrestrial DOM at the oxic/anoxic interface, thereby promoting its long-term sequestration. The exact
272 mechanisms of the Fe-DOM trapping in STEs are not well known. However, Linkhorst et al. (2018) showed
273 that the precipitation of amorphous Fe-oxides preferentially traps HMW compounds enriched in aromatic,
274 carboxylic, and hydroxyl moieties, such as altered lignin and polysaccharide compounds of terrestrial origin,
275 compared to the more aliphatic-rich compounds characteristic of marine DOM.

276 The DOC-CDOM decoupling observed along the permafrost-nearshore continuum (Fig. 5) suggested the
277 occurrence of distinct transformative processes between DOC and CDOM in beach groundwater and nearshore
278 waters, irrespective of salinity values. In the intertidal zone, the mixing between O₂-depleted beach groundwater
279 and well-oxygenated seawater induced suitable conditions for oxidative precipitation of Fe. In the absence of
280 light, microbial degradation and mineral-organic interactions likely dominated the fate of the flowing DOM
281 pool. As these processes operate simultaneously, they tend to decrease DOC and CDOM concentrations along
282 the continuum and change the degree of humification, lowering the molecular weight of the flowing material
283 (Fig. 4A to 4C). Despite this general trend, the impact on the aromaticity, as revealed by the SUVA values, is
284 less significant and surprisingly, the degree of aromaticity of the material tends to slightly increase along the
285 continuum. This suggests a higher proportion of aromatic compounds in the DOM pool. This increase is likely
286 due to the selective degradation of larger organic molecules by microbial and photochemical processes taking
287 place in the fresh-to-saltwater continuum (Benner and Amon, 2015). This increase could also be explained by
288 the preferential precipitation of non-humic material. As a result, the remaining DOM pool becomes dominated
289 by smaller, more aromatic compounds, thereby enhancing the overall aromaticity of the DOM. The low
290 fluorescent and biological indexes ($FI < 1.5$, $0.5 < BIX < 0.9$; data not shown) in nearshore water samples in
291 addition to high SUVA values indicated the occurrence of decomposed and more refractory DOM (McKnight



292 et al. 2001; Huguet et al. 2009) probably resulting from the large draining of the Mackenzie River. However,
293 the magnitude of the production of autochthonous DOM might be equivalent to the degradation processes,
294 which explains why the optical parameters in nearshore waters remain stable, regardless of the salinity. Indeed,
295 it suggests that freshly produced, protein-like FDOM (C2) from permafrost meltwater could be replaced by an
296 equivalent amount from local autochthonous sources, maintaining a consistent overall contribution of this DOM
297 despite variations in source origins.

298 ***3.4 Affinity with amorphous Fe-hydroxides and DOC-DOM decoupling***

299 The different affinity of DOC and CDOM₃₅₀ on Fe-hydroxides was experimentally tested by carrying out Fe-
300 spiked experiments of filtered meltwater, groundwater, and nearshore seawater samples. Here, the Fe-spiked
301 experiments were carried out to promote oxidative precipitation of amorphous Fe-hydroxides irrespective of
302 the total dissolved Fe concentrations measured in our samples (between the limit of detection to 680 $\mu\text{mol L}^{-1}$
303 in some groundwater samples). The sporadic presence of high Fe_{tot} concentration in beach groundwater samples
304 likely results from the redox oscillation tidally induced by the input of well-oxygenated seawater as currently
305 observed in STE systems (Charette et al., 2002, 2006).

306 In the Fe-spiked experiments, the initial DOC concentration of the seawater, groundwater and meltwater
307 samples were 383, 334 and 1019 $\mu\text{mol L}^{-1}$, respectively, in agreement with the median DOC values reported in
308 Fig. 4A for the different types of samples. As soon as Fe was added, the DOC concentrations dropped rapidly,
309 losing ~40% of initial concentrations. Then, the DOC concentrations decreased over the next hours, reaching
310 their lowest concentrations 6 hours after the start of the incubation (Fig. 6A). After 48 hours, however, the DOC
311 was gradually released in solution to reach a final concentration of 260, 219 and 710 $\mu\text{mol L}^{-1}$ for nearshore
312 seawater, beach groundwater, and meltwater samples, respectively. Since the experiment was conducted for
313 only 48 hours, it is uncertain whether DOC concentrations continued to increase beyond this point or if a plateau
314 was eventually reached. Over the 48h experiment, however, the DOC seemed to be gradually desorbed from
315 the Fe-mineral phase and the net loss of DOC in the solution was only 32%, 34% and 30% for nearshore
316 seawaters, beach groundwaters and meltwaters, respectively. The Fe-DOC trapping showed consistent



317 behaviour in all three sample types, indicating that the DOC pool reacted in the same way regardless of salinity.
318 In contrast, the loss of aCDOM₃₅₀ (or tDOM) in the solution was almost complete 6 hours after the Fe-spike
319 and the concentrations remained very low over the rest of the experiment (Fig 6B). At the end of the experiment,
320 the net tDOM loss was 62%, 57% and 94% of the initial content of nearshore seawaters, beach groundwaters
321 and meltwaters, respectively. The meltwaters exhibited the strongest tDOM loss in agreement with the initial
322 occurrence of HMW compounds with a high degree of humification, a material likely stabilized by amorphous
323 Fe. The preferential trapping of specific compounds during the transit favours the export of non-Fe-stabilized
324 material from beach groundwaters to nearshore seawaters. The DOC-CDOM decoupling observed along the
325 continuum might thus result from their different affinities on the amorphous Fe-mineral surface. The exact
326 mechanism controlling the molecular fractionation of the DOM pool in arctic groundwater remains to be
327 determined, and further studies are required to explore the role of Fe-curtain in arctic STEs.

328 *3.5 PARAFAC components in the DOM pool*

329 Among the three fluorescing peaks identified by the PARAFAC model, the C2 component mostly dominated
330 the FDOM pool whatever the type of samples and salinities (Fig.7). No significant trend in component
331 distribution was observed along the salinity gradient. The protein-like compound C2 was significantly
332 negatively correlated to C1 and C3 ($r^2=-0.89$, $p < 0.001$) and HIX ($r^2=-0.92$, $p < 0.001$) and the median values of
333 C2 increased along the continuum, the highest median value being in the nearshore seawater samples. The two
334 humic-like components (C1 and C3) were well correlated with each other ($r^2=0.81$, $p < 0.001$) and with HIX
335 ($r^2=0.85$ and 0.69 , respectively, $p < 0.001$). As observed for HIX, DOC and aCDOM₃₅₀, C1 and C3 decreased
336 along the continuum, with the lowest median values being measured in the seawater samples.

337 Upstream of the permafrost-nearshore continuum, massive ice and meltwater samples were mostly composed
338 of humic-like, HMW and terrestrially derived FDOM (C1) and they are rich in DOM and DOC, agreeing with
339 the active layer-derived FDOM also measured by Fouché et al. (2020). As the DOM transits, the loss of humic-
340 like compounds appears concomitant to the production of biologically-derived tyrosine-like FDOM, which is
341 typically produced by microbial organisms (Table 1 and references therein). The occurrence of non-Fe-



342 stabilized DOM and the redox conditions are then suitable for bacterial mineralization and the production of
343 lower MW and protein-like material. Bacterial mineralization of the transiting DOM is supported by the high
344 DIC concentrations measured in beach groundwater with concentrations higher than $3,000 \mu\text{mol L}^{-1}$ as observed
345 in samples collected in 2019 (Lizotte et al, 2022). Subterranean estuaries are biogeochemical reactors where
346 solutes of both marine and terrestrial origin are transformed and released to nearshore waters (Moore, 1999;
347 Anschutz et al., 2009). Moreover, a recent study in a subarctic beach suggested that the discharge zone may be
348 a hot spot of CO_2 degassing (Chaillou et al., 2024). The fraction of the permafrost-derived DOM which escaped
349 the Fe-curtain along the groundwater pathway was highly transformed through microbial degradation before
350 becoming diluted with the marine DOM pool.

351 **4 CONCLUSION**

352 In this study, we observed a rapid decrease in DOC and CDOM concentration across a short spatial scale,
353 indicating rapid and significant removal processes as DOM flows across the land-nearshore water continuum.
354 Microbial degradation and mineral-organic interactions would be preferentially removing HMW humic-like
355 material, leaving behind more aromatic, refractory compounds. Fe-hydroxides appear to play a key role in
356 rapidly and selectively trapping this tDOM during subsurface water transit, acting as a sink and shaping the
357 composition and concentration of DOM released in nearshore waters. The contribution of beach groundwater
358 and associated submarine discharge at the front of the coastal bluffs remains to be quantified, as it may regulate
359 carbon exports from permafrost watersheds to the Arctic Coastal Ocean.

360 Our findings highlight the role of intertidal and nearshore zones in regulating the persistence and reactivity of
361 terrestrial DOM as it transits from terrestrial to marine environments. The rapid loss of permafrost-derived
362 DOM in these environments, coupled with its interaction with mineral phases like amorphous iron oxides,
363 suggests that these zones may act as a permanent or transient terrestrial carbon sinks, as also observed in
364 temperate regions. However, the potential for rapid transformation and mineralization of this carbon along the
365 land-sea continuum indicates that much of it may be lost as CO_2 before reaching the ocean. This study



366 underscores the need for further research to understand the fate of DOM in Arctic coastal regions, particularly
367 in the context of accelerating permafrost thaw and coastal erosion. Further research is crucial for predicting the
368 impact of Arctic carbon fluxes on global biogeochemical cycles and developing strategies to mitigate the
369 consequences of permafrost degradation on climate systems. Given the ongoing effects of climate change, there
370 is an urgent need to comprehensively characterize and quantify these lateral and non-point source of carbon
371 within coastal Arctic budgets.

372 **Data availability:** Along with this submission, the dataset used in this research was submitted and accepted for
373 publication to Pangaea Data Publisher (www.pangaea.de). Once this article accepted for publication, the
374 moratorium in place will be lifted and the dataset generated during the study will be freely available in the
375 Pangaea repository. Here is the hyperlink and DOI toward the dataset:
376 <https://doi.pangaea.de/10.1594/PANGAEA.960986>

377 **Author contribution:** Aude Flamand: Investigation, Conceptualization, Methodology, Formal analysis,
378 Validation, Data curation, Visualization, Writing - Original Draft Preparation, Writing - Review & Editing;
379 Jean-François Lapierre: Supervision, Methodology, Validation, Data curation, Writing - Review & Editing;
380 Gwénaëlle Chaillou: Conceptualization, Methodology, Validation, Data curation, Supervision, Project
381 administration, Funding acquisition, Writing - Review & Editing.

382 **Competing interests:** The authors declare that there are no competing interests.

383 **Acknowledgements:** This project was made possible through the tremendous support of the hunters and
384 trappers committee, the hamlet and town council, in addition to several members of the Inuvialuit Nunangit
385 Sannaiqtuaq community of Tuktoyaktuk. The authors would like to express their gratitude to Dustin Whalen
386 (NRCan) for his invaluable contributions that made the fieldwork possible, as well as for his assistance in
387 providing resources and coordinating the fieldwork. We also want to thank Charlotte Irish, James Pokiak, Angus
388 Robertson, Bay Berry, and Brian Mayhew for their precious help during fieldwork in the summers of 2019 and
389 2021. We thank Claude Belzile for analyzing the DOC sample at ISMER-UQAR, Frédéric Bélanger for
390 conducting the CDOM and FDOM analysis of the 2019 samples and Antoine Biehler for his help with database



391 management. We also want to thank Simon Bélanger (UQAR) and Celine Guéguen (U. Sherbrooke) for
392 providing early feedback on this manuscript. This work represents a contribution to the scientific programs of
393 Nunataryuk, ArcticNet, and Québec-Océan.

394 **Financial support:** Financial support for this project has been provided by the Network of Centers of
395 Excellence of Canada ArcticNet (grant no. P-66), by Québec-Océan, funded through the Fonds de Recherche
396 du Québec – Nature et Technologies, and by the Aurora Research Institute – Aurora College. The authors
397 received additional funding from NSERC (RGPIN-2021-04332 to GC) and in-kind support from Natural
398 Resources Canada (Climate Change Geoscience Program and Polar Continental Shelf Program; grant no. 007-
399 19) for logistics support (equipment and helicopter time), and Crown–Indigenous Relations and Northern
400 Affairs Canada (Climate Change Preparedness in the North program, CCPN grant no. CCPN PN-NT-077-2018;
401 Beaufort Sea Regional Strategic Environmental Assessment Program, BRSEA agreement no. 239) in the form
402 of consultation tour of the ISR (March 2019). AF also received grants from the Northern Scientific Training
403 Program (NSTP) and from Québec-Océan.



404 **5 REFERENCES**

405 Anschutz, P., T. Smith, A. Mouret, J. Deborde, S. Bujan, D. Poirier, and P. Lecroart: Tidal sands as
406 biogeochemical reactors. *Estuarine, Coastal and Shelf Science* 84 (1): 84–90.
407 <https://doi.org/10.1016/j.ecss.2009.06.015>, 2009.

408 Benner, R., and Amon, R. M.: The size-reactivity continuum of major bioelements in the ocean, *Annu. Rev.*
409 *Mar. Sci.*, 7, 185–205, <https://doi.org/10.1146/annurev-marine-010213-135126>, 2015.

410 Berry, H. B., Whalen, D., and Lim, M.: Long-term ice-rich permafrost coast sensitivity to air temperatures and
411 storm influence: lessons from Pullen Island, Northwest Territories, Canada, *Arct. Sci.*, 7, 723–745,
412 <https://doi.org/10.1139/as-2020-0003>, 2021.

413 Bristol, E. M., Connolly, C. T., Lorensen, T. D., Richmond, B. M., Ilgen, A. G., Choens, R. C., Bull, D. L.,
414 Kanevskiy, M., Iwahana, G., and Jones, B. M.: Geochemistry of coastal permafrost and erosion-driven organic
415 matter fluxes to the Beaufort Sea near Drew Point, Alaska, *Front. Earth Sci.*, 8,
416 <https://doi.org/10.3389/FEART.2020.598933>, 2021.

417 Bro, R.: PARAFAC. Tutorial and applications, *Chemometr. Intell. Lab.*, 38, 149–171,
418 [https://doi.org/10.1016/S0169-7439\(97\)00032-4](https://doi.org/10.1016/S0169-7439(97)00032-4), 1997.

419 Chaillou, G., Lemay-Borduas, F., Larocque, M., Couturier, M., Biehler, A., and Tommi-Morin, G.: Flow and
420 discharge of groundwater from a snowmelt-affected sandy beach, *J. Hydrol.*, 557, 4–15,
421 <https://doi.org/10.1016/J.JHYDROL.2017.12.010>, 2018.

422 Chaillou, G., Tommi-Morin, G., and Mucci, A.: Production and fluxes of inorganic carbon and alkalinity in a
423 subarctic subterranean estuary, *Front. Mar. Sci.*, 11, <https://doi.org/10.3389/fmars.2024.1323463>, 2024.



- 424 Chaillou, G., Tommi-Morin, G., and Mucci, A. : Production and fluxes of inorganic carbon and alkalinity in a
425 subarctic subterranean estuary. *Front. Mar. Sci.* 11:1323463. <https://doi.org/10.3389/fmars.2024.1323463>,
426 2024.
- 427 Charette, M. A., and Sholkovitz, E. R.: Oxidative precipitation of groundwater-derived ferrous iron in the
428 subterranean estuary of a coastal bay, *Geophys. Res. Lett.*, 29, 85-81, <https://doi.org/10.1029/2001GL014512>,
429 2002.
- 430 Charrette, M. A., and Sholkovitz, E. R.: Trace element cycling in a subterranean estuary: Part 2.
431 Geochemistry of the pore water, *Geochim. Cosmochim. Ac.*, 70, 811–826,
432 <https://doi.org/10.1016/j.gca.2005.10.019>, 2006.
- 433 Couturier, M., Nozais, C., and Chaillou, G.: Microtidal subterranean estuaries as a source of fresh terrestrial
434 dissolved organic matter to the coastal ocean, *Mar. Chem.*, 186, 46–57,
435 <https://doi.org/10.1016/j.marchem.2016.08.001>, 2016.
- 436 Del Vecchio, R., and Blough, N. V.: Spatial and seasonal distribution of chromophoric dissolved organic
437 matter and dissolved organic carbon in the Middle Atlantic Bight, *Mar. Chem.*, 89, 169–187,
438 <https://doi.org/10.1016/j.marchem.2004.02.027>, 2004.
- 439 Frenette, J-J., Massicotte, P., and Lapierre, J-F.: Colorful Niches of Phytoplankton Shaped by the Spatial
440 Connectivity in a Large River Ecosystem: A Riverscape Perspective. *PLoS ONE*, 7(4), e35891,
441 <https://doi.org/10.1371/journal.pone.0035891>, 2012.
- 442 Fichot, C. G., and Benner, R.: A novel method to estimate DOC concentrations from CDOM absorption
443 coefficients in coastal waters, *Geophys. Res. Lett.*, 38, <https://doi.org/10.1029/2010GL046152>, 2011.



- 444 Fichot, C. G., Kaiser, K., Hooker, S. B., Amon, R. M. W., Babin, M., Bélanger, S., Walker, S. A., and
445 Benner, R.: Pan-Arctic distributions of continental runoff in the Arctic Ocean, *Sci. Rep.-UK*, 3, 1053,
446 <https://doi.org/10.1038/srep01053>, 2013.
- 447 Fichot, C. G., and Benner, R.: The fate of terrigenous dissolved organic carbon in a river-influenced ocean
448 margin, *Global Biogeochem. Cy.*, 28, 300–318, <https://doi.org/10.1002/2013GB004670>, 2014.
- 449 Fouché, J., Christiansen, C. T., Lafrenière, M. J., Grogan, P., and Lamoureux, S. F.: Canadian permafrost stores
450 large pools of ammonium and optically distinct dissolved organic matter, *Nat. Commun.*, 11, 4500,
451 <https://doi.org/10.1038/s41467-020-18331-w>, 2020.
- 452 Fritz, M., Wetterich, S., Meyer, H., Schirrmeister, L., Lantuit, H., and Pollard, W. H.: Origin and characteristics
453 of massive ground ice on Herschel Island (western Canadian Arctic) as revealed by stable water isotope and
454 hydrochemical signatures, *Permafrost Periglac.*, 22, 26–38, <https://doi.org/10.1002/ppp.714>, 2011.
- 455 Fritz, M., Vonk, J. E., and Lantuit, H.: Collapsing Arctic coastlines, *Nat. Clim. Change*, 7, 6–7,
456 <https://doi.org/10.1038/nclimate3188>, 2017.
- 457 Fritz, M., Wetterich, S., McAlister, J., and Meyer, H.: A new local meteoric water line for Inuvik (NT, Canada),
458 *Earth Syst. Sci. Data*, 14, 57–63, <https://doi.org/10.5194/essd-14-57-2022>, 2022.
- 459 Guo, L., Ping, C. L., and Macdonald, R. W.: Mobilization pathways of organic carbon from permafrost to
460 arctic rivers in a changing climate, *Geophys. Res. Lett.*, 34, <https://doi.org/10.1029/2007GL030689>, 2007.
- 461 Hansen, A.M., Kraus, T.E.C., Pellerin, B.A., Fleck, J.A., Downing, B.D. and Bergamaschi, B.A.: Optical
462 properties of dissolved organic matter (DOM): Effects of biological and photolytic degradation. *Limnol.*
463 *Oceanogr.*, 61: 1015-1032. <https://doi.org/10.1002/lno.10270>, 2016.



- 464 Hayes, S., Lim, M., Whalen, D., Mann, P. J., Fraser, P., Penlington, R., and Martin, J.: The role of massive ice
465 and exposed headwall properties on retrogressive thaw slump activity. *J. Geophys. Res. Earth Surf.*, 127,
466 e2022JF006602. <https://doi.org/10.1029/2022JF006602>, 2022.
- 467 Hayes, S.: Massive ice and topographic controls on retrogressive thaw slump dynamics: Peninsula point,
468 western canadian arctic (Order No. 28187262). Doctoral thesis, Northumbria University. from Northumbria
469 Research Link: <http://nrl.northumbria.ac.uk/id/eprint/44081/>, 2020.
- 470 Hébert, A.-J., Flaman, A., and Chaillou, G.: Origins and transformations of terrigenous dissolved organic
471 matter in a transgressive coastal system, *Estuar. Coast. Shelf S.*, 279, 108137,
472 <https://doi.org/10.1016/J.ECSS.2022.108137>, 2022.
- 473 Hedges, J. I., and Keil, R. G.: Sedimentary organic matter preservation: an assessment and speculative
474 synthesis, *Mar. Chem.*, 49, 81–115, [https://doi.org/10.1016/0304-4203\(95\)00008-F](https://doi.org/10.1016/0304-4203(95)00008-F), 1995.
- 475 Helms, J. R., Stubbins, A., Ritchie, J. D., Minor, E. C., Kieber, D. J., and Mopper, K.: Absorption spectral
476 slopes and slope ratios as indicators of molecular weight, source, and photobleaching of chromophoric dissolved
477 organic matter, *Limnol. Oceanogr.*, 53, 955–969, <https://doi.org/10.4319/LO.2008.53.3.0955>, 2008.
- 478 Huguet, A., Vacher, L., Relexans, S., Saubusse, S., Froidefond, J.-M., and Parlanti, E.: Properties of fluorescent
479 dissolved organic matter in the Gironde Estuary, *Org. Geochem.*, 40, 706–719,
480 <https://doi.org/10.1016/j.orggeochem.2009.03.002>, 2009.
- 481 Jones, B. M., Irrgang, A. M., Farquharson, L. M., Lantuit, H., Whalen, D., Ogorodov, S., Grigoriev, M.,
482 Tweedie, C., Gibbs, A. E., Strzelecki, M. C., Baranskaya, A., Belova, N., Sinitsyn, A., Kroon, A., Maslakov,
483 A., Vieira, G., Grosse, G., Overduin, P., Nitze, I., Maio, C., Overbeck, J., Bendixen, M., Zagórski, P., and
484 Romanovsky, V. E.: Arctic Report Card 2020: Coastal Permafrost Erosion, [https://doi.org/10.25923/e47w-](https://doi.org/10.25923/e47w-dw52)
485 [dw52](https://doi.org/10.25923/e47w-dw52), 2020.



- 486 Kaiser, K., Benner, R., and Amon, R. M. W.: The fate of terrigenous dissolved organic carbon on the Eurasian
487 shelves and export to the North Atlantic, *J. Geophys. Res.-Oceans*, 122, 4–22,
488 <https://doi.org/10.1002/2016jc012380>, 2017a.
- 489 Kaiser, K., Canedo-Oropeza, M., McMahon, R., and Amon, R. M. W.: Origins and transformations of dissolved
490 organic matter in large Arctic rivers, *Sci. Rep.*, 7, <https://doi.org/10.1038/s41598-017-12729-1>, 2017b.
- 491 Kipp, L. E., Charette, M. A., Moore, W. S., Henderson, P. B., and Rigor, I. G.: Increased fluxes of shelf-
492 derived materials to the central arctic ocean, *Sci. Adv.*, 4, <https://doi.org/10.1126/SCIADV.AAO1302>, 2018.
- 493 Kipp, L. E., Chaillou, G., Kienast, M., Tamborski, J., and Whalen, D. : On the utility of radium isotopes as
494 tracers of massive ice-derived solutes in a changing Arctic. *Geochim. Cosmochim. Acta.* submitted.
- 495 Kwasigroch, U., Beldowska, M., Jędruch, A., and Saniewska, D.: Coastal erosion—a “new” land-based source
496 of labile mercury to the marine environment, *Environ. Sci. Pollut. Res.*, 25, 28682–28694,
497 <https://doi.org/10.1007/S11356-018-2856-7/FIGURES/4>, 2018.
- 498 Lantuit, H., Overduin, P. P., Couture, N., Wetterich, S., Aré, F., Atkinson, D., Brown, J., Cherkashov, G.,
499 Drozdov, D., Donald Forbes, L., Graves-Gaylord, A., Grigoriev, M., Hubberten, H. W., Jordan, J., Jorgenson,
500 T., Ødegård, R. S., Ogorodov, S., Pollard, W. H., Rachold, V., Sedenko, S., Solomon, S., Steenhuisen, F.,
501 Streletskaia, I., and Vasiliev, A.: The Arctic Coastal Dynamics Database: A New Classification Scheme and
502 Statistics on Arctic Permafrost Coastlines, *Estuaries Coasts*, 35, 383–400, [https://doi.org/10.1007/S12237-](https://doi.org/10.1007/S12237-010-9362-6)
503 [010-9362-6](https://doi.org/10.1007/S12237-010-9362-6), 2012.
- 504 Lecher, A.L.: Groundwater Discharge in the Arctic: A Review of Studies and Implications for
505 Biogeochemistry, *Hydrol.* ,4(3),41, <https://doi.org/10.3390/hydrology4030041>, 2017.



- 506 Li, Q., Hu, W., Li, L., and Li, Y.: Interactions between organic matter and Fe oxides at soil micro-interfaces:
507 Quantification, associations, and influencing factors, *Sci. Total Environ.*, 855,
508 <https://doi.org/10.1016/j.scitotenv.2023.158710>, 2023.
- 509 Linkhorst, A., Dittmar, T., and Waska, H.: Molecular Fractionation of Dissolved Organic Matter in a Shallow
510 Subterranean Estuary: The Role of the Iron Curtain, *Environ. Sci. Technol.*, 51, 1312–1320,
511 <https://doi.org/10.1021/acs.est.6b03608>, 2017.
- 512 Lizotte, M., Juhls, B., Matsuoka, A., Massicotte, P., Mével, G., Anikina, D. O. J., Antonova, S., Bécu, G.,
513 Béguin, M., Bélanger, S., Bossé-Demers, T., Bröder, L., Bruyant, F., Chaillou, G., Comte, J., Couture, R.-M.,
514 Devred, E., Deslongchamps, G., Dezutter, T., Dillon, M., Doxaran, D., Flamand, A., Fell, F., Ferland, J., Forget,
515 M.-H., Fritz, M., Gordon, T. J., Guilmette, C., Hilborn, A., Hussherr, R., Irish, C., Joux, F., Kipp, L., Laberge-
516 Carignan, A., Lantuit, H., Leymarie, E., Mannino, A., Maury, J., Overduin, P., Oziel, L., Stedmon, C., Thomas,
517 C., Tisserand, L., Tremblay, J.-É., Vonk, J., Whalen, D., and Babin, M.: Nunataryuk field campaigns:
518 Understanding the origin and fate of terrestrial organic matter in the coastal waters of the Mackenzie Delta
519 region, *Earth Syst. Sci. Data*, 15, 1617–1653, <https://doi.org/10.5194/essd-2022-163>, 2023.
- 520 Macdonald, R. W., Solomon, S. M., Cranston, R. E., Welch, H. E., Yunker, M. B., and Gobeil, C.: A sediment
521 and organic carbon budget for the Canadian Beaufort Shelf, *Mar. Geol.*, 144, 255–273,
522 [https://doi.org/10.1016/S0025-3227\(97\)00106-0](https://doi.org/10.1016/S0025-3227(97)00106-0), 1998.
- 523 Mackay, J.R.: Fifty years (1935-1985) of coastal retreat west of Tuktoyaktuk, District of Mackenzie, Geological
524 Survey of Canada, 86-1A, 727–735, 1986.
- 525 Massicotte, P., Asmala, E., Stedmon, C., and Markager, S.: Global distribution of dissolved organic matter
526 along the aquatic continuum: Across rivers, lakes and oceans, *Sci. Total Environ.*, 609, 180–191,
527 <https://doi.org/10.1016/j.scitotenv.2017.07.076>, 2017.



- 528 Matsuoka, A., Bricaud, A., Benner, R., Para, J., Sempéré, R., Prieur, L., Bélanger, S., and Babin, M.: Tracing
529 the transport of colored dissolved organic matter in water masses of the Southern Beaufort Sea: relationship
530 with hydrographic characteristics, *Biogeosciences*, 9, 925–940, <https://doi.org/10.5194/bg-9-925-2012>, 2012.
- 531 McKnight, D. M., Boyer, E. W., Westerhoff, P. K., Doran, P. T., Kulbe, T., and Andersen, D. T.:
532 Spectrofluorometric characterization of dissolved organic matter for indication of precursor organic material
533 and aromaticity, *Limnol. Oceanogr.*, 46, 38–48, <https://doi.org/10.4319/lo.2001.46.1.0038>, 2001.
- 534 McMeans, B. C., McCann, K. S., Humphries, M., Rooney, N., and Fisk, A. T.: Food Web Structure in
535 Temporally-Forced Ecosystems, *Trends Ecol. Evol.*, 30, 662–672,
536 <https://doi.org/10.1016/J.TREE.2015.09.001>, 2015.
- 537 Meilleur, C., Kamula, M., Kuzyk, Z. A., and Guéguen, C.: Insights into surface circulation and mixing in James
538 Bay and Hudson Bay from dissolved organic matter optical properties, *J. Mar. Syst.*, 238, 103841,
539 <https://doi.org/10.1016/J.JMARSYS.2022.103841>, 2023.
- 540 Moore, W. S.: The subterranean estuary: a reaction zone of ground water and sea water, *Mar. Chem.*, 65(1–2),
541 111–125, doi:10.1016/S0304-4203(99)00014-6, 1999.
- 542 Moore, W. S., Benitez-Nelson, C., Schutte, C., Moody, A., Shiller, A., Sibert, R. J., and Joye, S.: SGD-OD:
543 investigating the potential oxygen demand of submarine groundwater discharge in coastal systems, *Sci. Rep.*,
544 14, 9249, <https://doi.org/10.1038/s41598-024-59229-7>, 2024.
- 545 Murphy, K. R., Stedmon, C. A., Graeber, D., and Bro, R.: Fluorescence spectroscopy and multi-way techniques.
546 PARAFAC, *Anal. Methods*, 5, <https://doi.org/10.1039/c3ay41160e>, 2013.



- 547 Nelson, N. B., Siegel, D. A., and Michaels, A. F.: Seasonal dynamics of colored dissolved material in the
548 Sargasso Sea, *Deep Sea Res. Part I Oceanogr. Res. Pap.*, 45, 931–957, <https://doi.org/10.1016/S0967->
549 0637(97)00106-4, 1998.
- 550 Nelson, N. B., and Siegel, D. A.: The global distribution and dynamics of chromophoric dissolved organic
551 matter, *Annu. Rev. Mar. Sci.*, 5, 447–476, <https://doi.org/10.1146/annurev-marine-120710-100751>, 2013.
- 552 Obu, J., Westermann, S., Bartsch, A., Berdnikov, N., Christiansen, H. H., Dashtseren, A., Delaloye, R.,
553 Elberling, B., Etzelmüller, B., Kholodov, A., Khomutov, A., Kääh, A., Leibman, M. O., Lewkowicz, A. G.,
554 Panda, S. K., Romanovsky, V., Way, R. G., Westergaard-Nielsen, A., Wu, T., Yamkhin, J., and Zou, D.:
555 Northern Hemisphere permafrost map based on TTOP modelling for 2000–2016 at 1 km² scale, *Earth-Sci.*
556 *Rev.*, 193, 299–316, <https://doi.org/10.1016/j.earscirev.2019.04.023>, 2019.
- 557 Ohno, T.: Fluorescence Inner-Filtering Correction for Determining the Humification Index of Dissolved
558 Organic Matter, *Environ. Sci. Technol.*, 36 (4), 742–746, <https://doi.org/10.1021/es0155276>, 2002.
- 559 Ouellette, D. S.: Thermal and Mechanical Modeling of Coastal Erosion Processes on Tuktoyaktuk Island,
560 Northwest Territories, Master thesis, University of Calgary, Calgary, Canada, 2021.
- 561 Pucher, M., Wunsch, U., Weigelhofer, G., Murphy, K., Hein, T., and Graeber, D.: staRdom: Versatile Software
562 for Analyzing Spectroscopic Data of Dissolved Organic Matter in R, *Water*, 11, 2366,
563 <https://doi.org/10.3390/w11112366>, 2019.
- 564 Riedel, T., Zak, D., Biester, H., and Dittmar, T.: Iron traps terrestrially derived dissolved organic matter at redox
565 interfaces, *PNAS*, 110, 10101–10105, <https://doi.org/10.1073/pnas.1221487110>, 2013.
- 566 Schuur, E. A. G., McGuire, A. D., Schädel, C., Grosse, G., Harden, J. W., Hayes, D. J., Hugelius, G., Koven,
567 C. D., Kuhry, P., Lawrence, D. M., Natali, S. M., Olefeldt, D., Romanovsky, V. E., Schaefer, K., Turetsky, M.



- 568 R., Treat, C. C., and Vonk, J. E.: Climate change and the permafrost carbon feedback, *Nature*, 520, 171–179,
569 <https://doi.org/10.1038/nature14338>, 2015.
- 570 Sirois, M., Couturier, M., Barber, A., Gélinas, Y., and Chaillou, G.: Interactions between iron and organic
571 carbon in a sandy beach subterranean estuary, *Mar. Chem.*, 202, 86–96,
572 <https://doi.org/10.1016/j.marchem.2018.02.004>, 2018.
- 573 Solomon, S. M.: Spatial and temporal variability of shoreline change in the Beaufort-Mackenzie region,
574 northwest territories, Canada, *Geo-Mar. Lett.*, 25, 127–137, <https://doi.org/10.1007/S00367-004-0194-X>, 2005.
- 575 Spencer, R. G., Aiken, G. R., Dornblaser, M. M., Butler, K. D., Holmes, R. M., Fiske, G., and Stubbins, A.:
576 Chromophoric dissolved organic matter export from US rivers, *Geophys. Res. Lett.*, 40, 1575–1579,
577 <https://doi.org/10.1002/grl.50357>, 2013.
- 578 Stedmon, C. A., Amon, R. M. W., Rinehart, A. J., and Walker, S. A.: The supply and characteristics of colored
579 dissolved organic matter (CDOM) in the Arctic Ocean: Pan Arctic trends and differences, *Mar. Chem.*, 124,
580 108–118, <https://doi.org/10.1016/j.marchem.2010.12.007>, 2011.
- 581 Stedmon, C. A., Markager, S., and Bro, R.: Tracing dissolved organic matter in aquatic environments using a
582 new approach to fluorescence spectroscopy, *Mar. Chem.*, 82, 239–254, [https://doi.org/10.1016/s0304-](https://doi.org/10.1016/s0304-4203(03)00072-0)
583 [4203\(03\)00072-0](https://doi.org/10.1016/s0304-4203(03)00072-0), 2003.
- 584 Stookey, L. L.: Ferrozine—A New Spectrophotometric Reagent for Iron, *Anal. Chem.*, 42, 779–781,
585 <https://doi.org/10.1021/AC60289A016>, 1970.
- 586 Tanguy, R., Whalen, D., Prates, G., and Vieira, G.: Shoreline change rates and land to sea sediment and soil
587 organic carbon transfer in eastern Parry Peninsula from 1965 to 2020 (Amundsen Gulf, Canada), *Arctic Sci.*,
588 1–20, <https://doi.org/10.1139/as-2022-0028>, 2023.



- 589 Thingstad, T. F., Bellerby, R. G. J., Bratbak, G., Børsheim, K. Y., Egge, J. K., Heldal, M., Larsen, A., Neill,
590 C., Nejstgaard, J., Norland, S., Sandaa, R. A., Skjoldal, E. F., Tanaka, T., Thyrhaug, R., and Töpper, B.:
591 Counterintuitive carbon-to-nutrient coupling in an Arctic pelagic ecosystem, *Nature*, 455, 387–390,
592 <https://doi.org/10.1038/nature07235>, 2008.
- 593 Utting, N., Clark, I., Lauriol, B., Wieser, M., and Aeschbach-Hertig, W.: Origin and Flow Dynamics of
594 Perennial Groundwater in Continuous Permafrost Terrain using Isotopes and Noble Gases: Case Study of the
595 Fishing Branch River, Northern Yukon, Canada, *Permafrost Periglac.*, 23, 91–106,
596 <https://doi.org/10.1002/ppp.1732>, 2012.
- 597 Viollier, E., Inglett, P. W., Hunter, K., Roychoudhury, A. N., and Van Cappellen, P.: The ferrozine method
598 revisited: Fe(II)/Fe(III) determination in natural waters, *Appl. Geochem.*, 15, 785–790,
599 [https://doi.org/10.1016/S0883-2927\(99\)00097-9](https://doi.org/10.1016/S0883-2927(99)00097-9), 2000.
- 600 Vonk, J. E., Semiletov, I. P., Dudarev, O. V., Eglinton, T. I., Andersson, A., Shakhova, N., Charkin, A., Heim,
601 B., and Gustafsson, Ö.: Preferential burial of permafrost-derived organic carbon in Siberian-Arctic shelf waters,
602 *J. Geophys. Res.: Oceans*, 119, 8410–8421, <https://doi.org/10.1002/2014JC010261>, 2014.
- 603 Vonk, J. E., Tank, S. E., Bowden, W. B., Laurion, I., Vincent, W. F., Alekseychik, P., Amyot, M., Billet, M.
604 F., Canário, J., Cory, R. M., Deshpande, B. N., Helbig, M., Jammet, M., Karlsson, J., Larouche, J.,
605 Macmillan, G., Rautio, M., Walter Anthony, K. M., and Wickland, K. P.: Reviews and syntheses: Effects of
606 permafrost thaw on Arctic aquatic ecosystems, *Biogeosciences*, 12, 7129–7167, [https://doi.org/10.5194/bg-](https://doi.org/10.5194/bg-12-7129-2015)
607 12-7129-2015, 2015.
- 608 Walvoord, M. A., and Striegl, R. G.: Increased groundwater to stream discharge from permafrost thawing in
609 the Yukon River basin: Potential impacts on lateral export of carbon and nitrogen, *Geophys. Res. Lett.*, 34,
610 <https://doi.org/10.1029/2007gl030216>, 2007.



- 611 Waska, H., Simon, H., Ahmerkamp, S., Greskowiak, J., Ahrens, J., Seibert, S. L., Schwalfenberg, K.,
612 Zielinski, O., and Dittmar, T.: Molecular traits of dissolved organic matter in the subterranean estuary of a
613 high-energy beach: Indications of sources and sinks, *Front. Mar. Sci.*, 8, 54,
614 <https://doi.org/10.3389/FMARS.2021.607083/BIBTEX>, 2021.
- 615 Weishaar, J. L., Aiken, G. R., Bergamaschi, B. A., Fram, M. S., Fujii, R., and Mopper, K.: Evaluation of
616 specific ultraviolet absorbance as an indicator of the chemical composition and reactivity of dissolved organic
617 carbon, *Environ. Sci. Technol.*, 37, 4702–4708, <https://doi.org/10.1021/es030360x>, 2003.
- 618 Whalen, D., Forbes, D. L., Kostylev, V., Lim, M., Fraser, P., Nedimović, M. R., and Stuckey, S.: Mechanisms,
619 volumetric assessment, and prognosis for rapid coastal erosion of Tuktoyaktuk Island, an important natural
620 barrier for the harbour and community, *Can. J. Earth Sci.*, 59, 945–960, <https://doi.org/10.1139/cjes-2021-0101>,
621 2022.
- 622 Wurl, O., and Tsai, M. S.: Analysis of Dissolved and Particulate Organic Carbon with the HTCO Technique,
623 in: *Practical Guidelines for the Analysis of Seawater*, CRC Press, pp. 45–60, 2009.
- 624 Zhou, Z., Henkel, S., Kasten, S., and Holtappels, M.: The iron “redox battery” in sandy sediments: Its impact
625 on organic matter remineralization and phosphorus cycling. *Sci. Total. Environ.*, 865, 161168,
626 <https://doi.org/10.1016/j.scitotenv.2022.161168>, 2023.
- 627 Zhou, Z., Waska, H., Henkel, S., Dittmar, T., Kasten, S., and Holtappels, M.: Iron promotes the retention of
628 terrigenous Dissolved organic matter in subtidal Permeable Sediments. *Environ. Sci. Technol.*, 58, 6204–6214,
629 <https://doi.org/10.1021/acs.est.3c09531>, 2024.
- 630



631 **TABLES**

632 Table 1: Description of the EEM-PARAFAC modelled FDOM components based on the literature results of
 633 literature references. PARAFAC components and their characteristics

634

Comp.	Peak max Ex/Em	Coble peak	Description	Literature
C1	250-335/466	A, C	Humic-like terrestrial, HMW, aromatic	C _C : <240-340/452 (Olefelt et al., 2014) ALL1: 250-350/459 (Pitta and Zeri 2021) C3: <240-355/476 (Stedmon and Markager, 2005a) C3: 260-370/490 (Murphy et al., 2018) C4: <255-360/460 (Fouché et al., 2020)
C2	265/296	B	Protein-like, tyrosine, biological, microbial autochthonous origin. LMW phenolic compounds.	C _T : 270/<300 (Olefelt et al., 2014) ACT-10 C3: 270/302 (D'Andrilli and McConnell 2021) C6: 280/338 (Stedmon and Markager, 2005a) C1:275/<300 (Murphy et al. 2008) C1: 275/306 (Fouché et al., 2020)
C3	250-295/414	A, M	Humic-like, terrestrial, autochthonous production and microbial processing, LMW.	C _M :<240,305/404 (Olefelt, Persson et al. 2014) C2: <300/396 (Sondergaard, Stedmon et al. 2003) C2 : 315/418 (Murphy et al., 2008) C2: 310/ 415 (Fouché et al., 2020)

635

636

637

638

639

640

641

642

643



646 **FIGURE CAPTIONS**

647 **Fig. 1** Map of the four sampling sites (red dots) located in the Northwest Territories, Canada.

648 **Fig. 2** EEMs of the 3-components PARAFAC model. Fluorescence is expressed in Raman Unit (R.U.).

649 **Fig. 3** Isotopic composition of massive ice, meltwater, beach groundwater and seawater samples collected in
650 2019 showing the mixing line between samples across the salinity gradient, from the meltwater to the
651 seawater. global (GMWL; Craig, 1961) and the local meteoric water line for Inuvik (LMWL, Fritz et al.,
652 2022) are also reported. Note that only one massive ice sample (N=1) was collected.

653 **Fig. 4** Distribution of (A) DOC, (B) CDOM₃₅₀, (C) HIX and (D) SUVA₂₅₄ indexes in the salinity gradient
654 and for the different types of collected samples (*i.e.*, beach groundwater, massive ice, meltwater and
655 nearshore seawater samples). Note that there is only one massive ice sample reported here. For the boxplots,
656 the black lines are the median values, the whiskers are the extent of the data, and the dot points are the outlier
657 values.

658 **Fig. 5** Global relationship between absorption coefficients at 350 nm (aCDOM₃₅₀ in m⁻¹) and DOC
659 concentrations (in μmol L⁻¹) along the permafrost to nearshore aquatic continuum. Note that the data is
660 reported in Log units.

661 **Fig. 6** Behaviour of (A) DOC and (B) aCDOM₃₅₀ concentrations with excess iron and constant oxygenation
662 in the different type of samples incubated over 48 hours. The non-colored points represent the concentrations
663 before the addition of Fe-spike at t=0h.

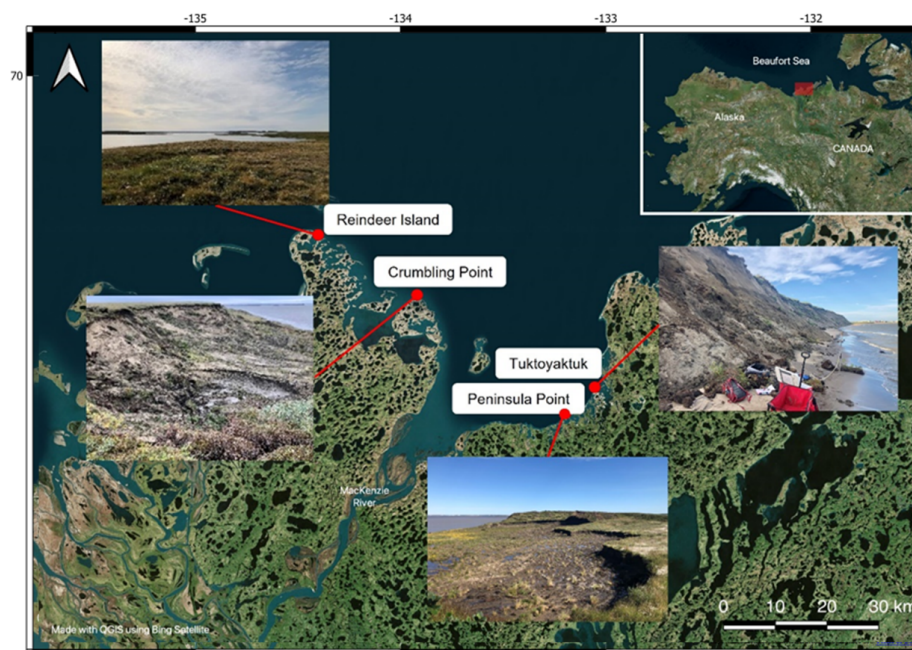
664 **Fig. 7** Distribution of PARAFAC components (A) C1, (B) C2, and (C) C3 along the salinity gradient and for
665 the different types of collected samples (*i.e.*, beach groundwater, massive ice, meltwater and nearshore
666 seawater samples). Note that there is only one massive ice sample reported here. For the boxplots, the black



667 lines represent the median values, the whiskers represent the extent of the data, and the dot points represent

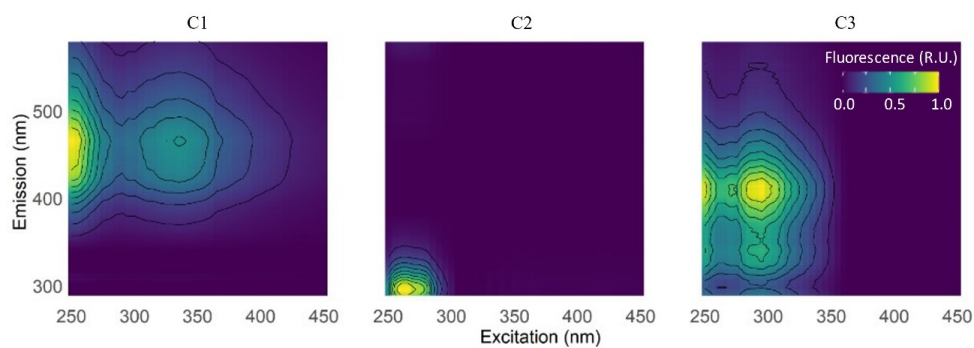
668 the outlier values.

669



670

671 **Fig. 1** Map of the four sampling sites (red dots) located in the Northwest Territories, Canada.

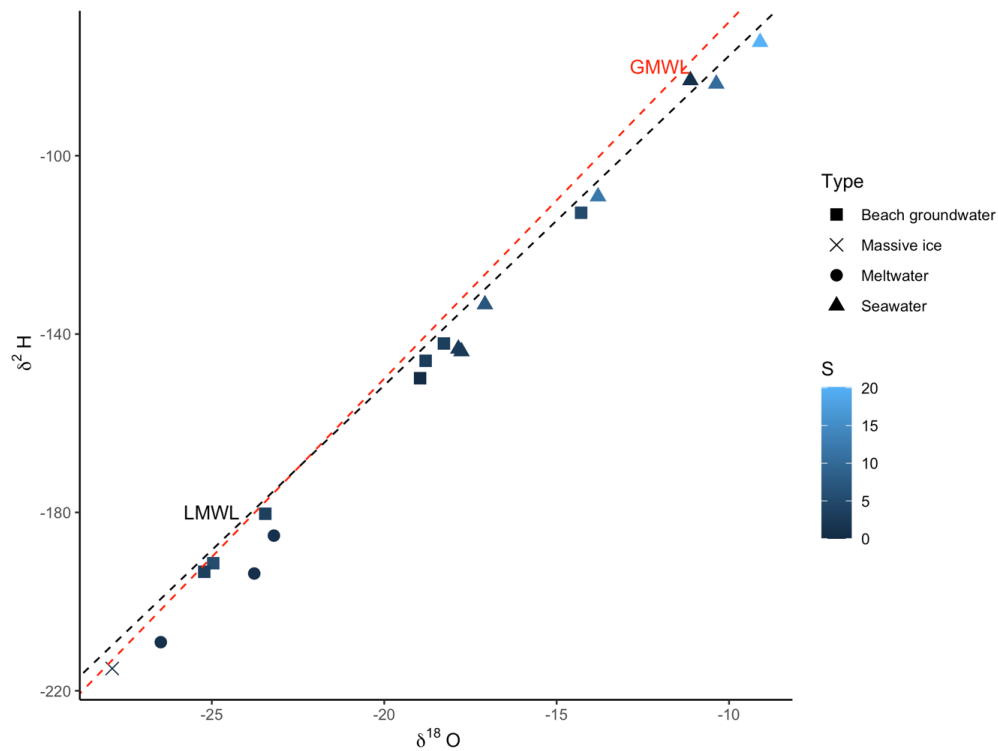


672

673 **Fig. 2** EEMs of the 3-components PARAFAC model. Fluorescence is expressed in Raman Unit (R.U.).

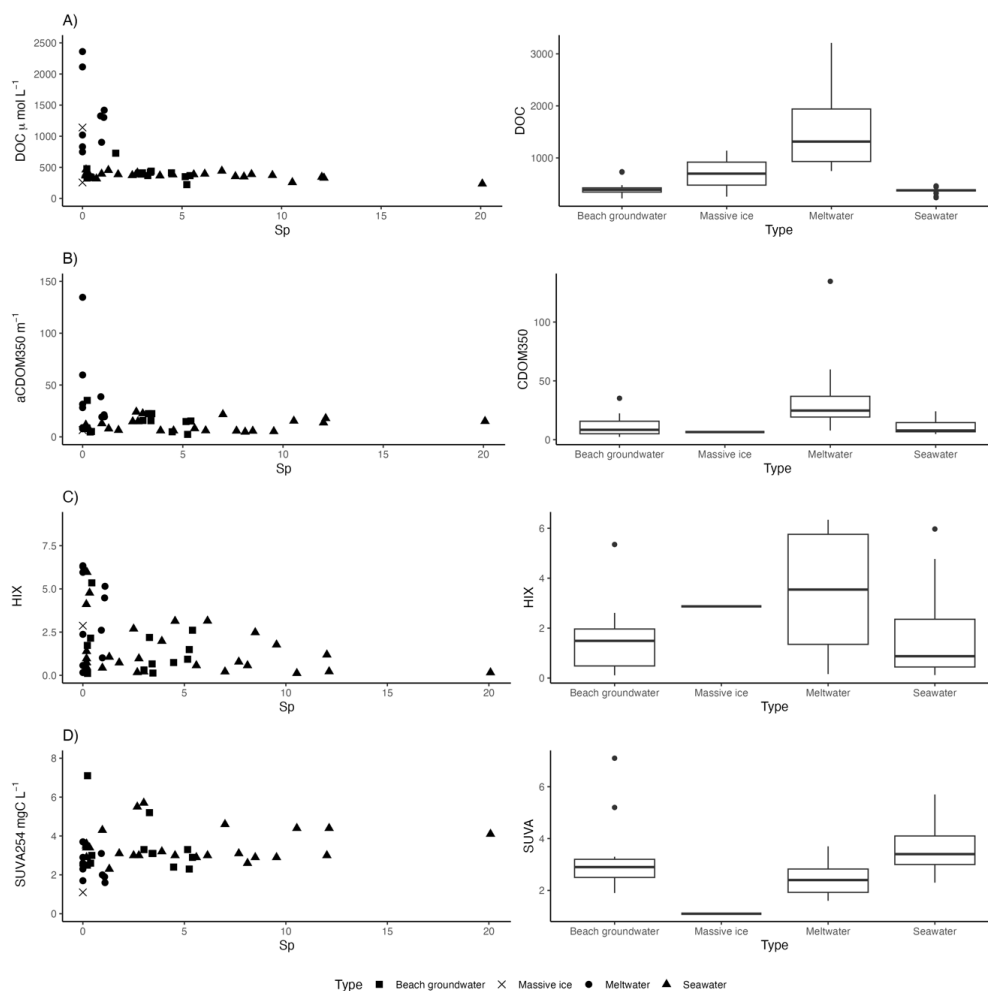
674

675



676

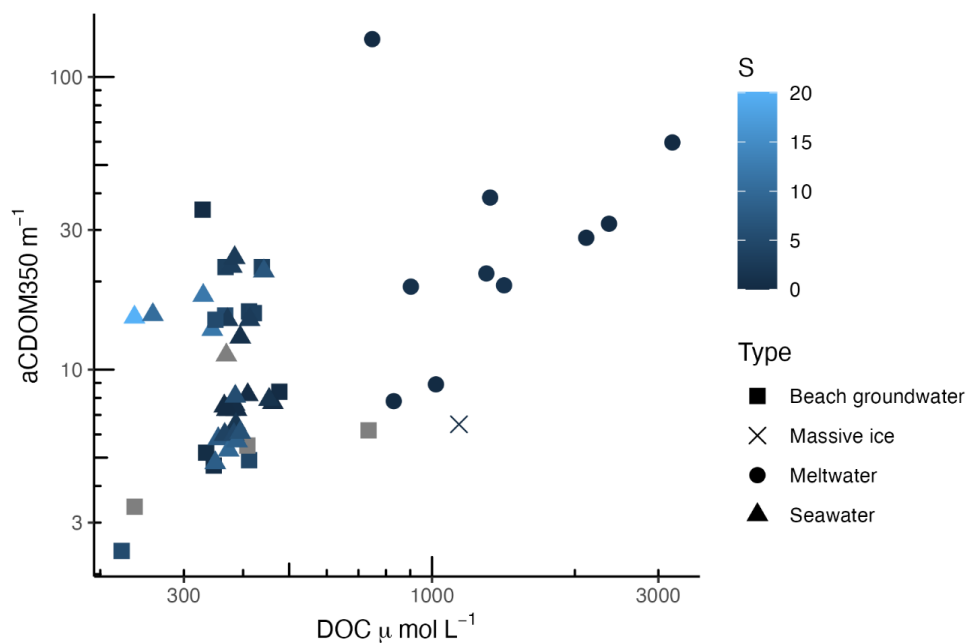
677 **Fig. 3** Isotopic composition of massive ice, meltwater, beach groundwater and seawater samples collected in
678 2019 showing the mixing line between samples across the salinity gradient, from the meltwater to the
679 seawater. global (GMWL; Craig, 1961) and the local meteoric water line for Inuvik (LMWL, Fritz et al.,
680 2022) are also reported. Note that only one massive ice sample (N=1) was collected.



681

682 **Fig. 4** Distribution of (A) DOC, (B) CDOM350, (C) HIX and (D) SUVA254 indexes in the salinity gradient
683 and for the different types of collected samples (*i.e.*, beach groundwater, massive ice, meltwater and
684 nearshore seawater samples). Note that there is only one massive ice sample reported here. For the boxplots,
685 the black lines are the median values, the whiskers are the extent of the data, and the dot points are the outlier
686 values.

687



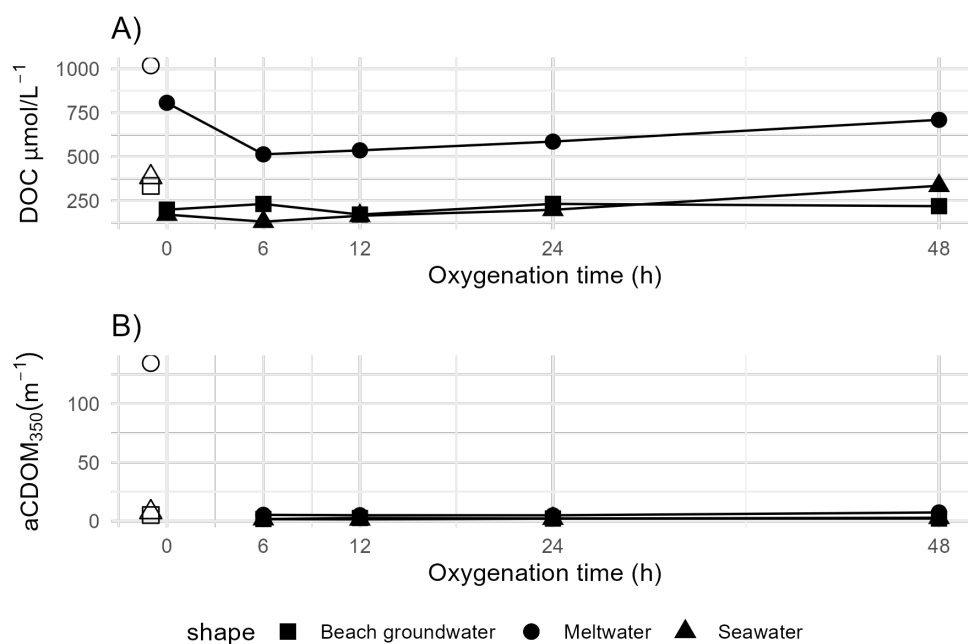
688

689 **Fig. 5** Global relationship between absorption coefficients at 350 nm ($a\text{CDOM}_{350}$ in m^{-1}) and DOC
690 concentrations (in $\mu\text{mol L}^{-1}$) along the permafrost to nearshore aquatic continuum. Note that the data is
691 reported in Log units.

692



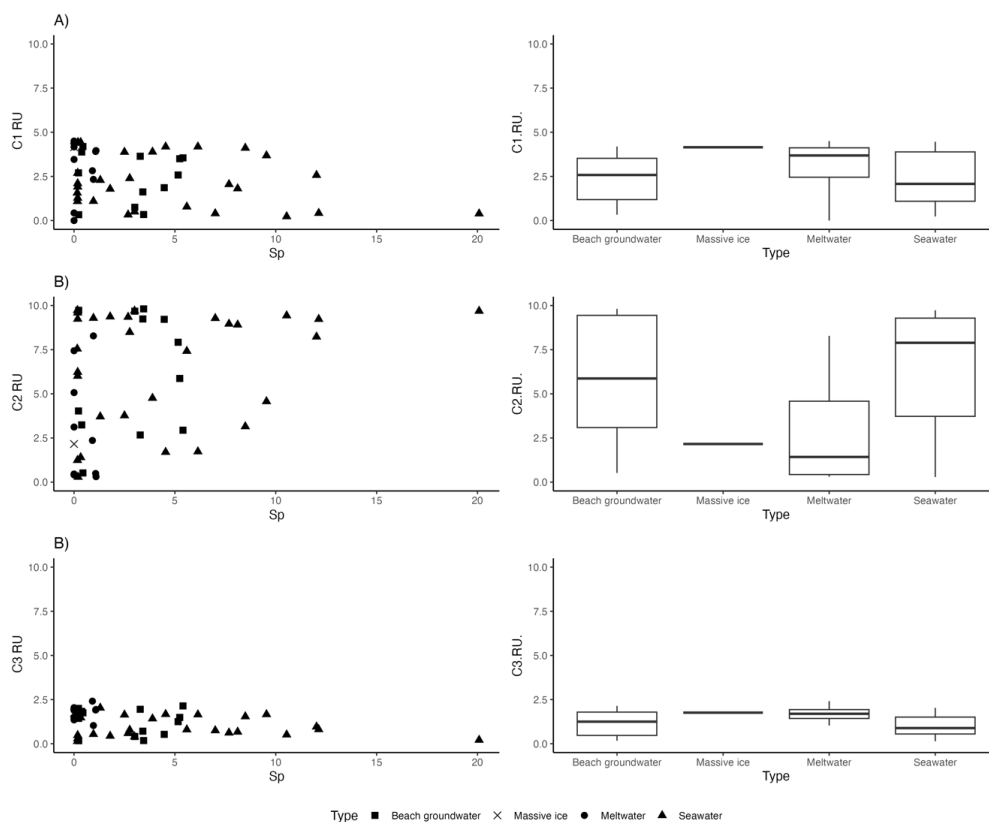
693



694

695 **Fig. 6** Behaviour of (A) DOC and (B) aCDOM₃₅₀ concentrations with excess iron and constant oxygenation
696 in the different type of samples incubated over 48 hours. The non-colored points represent the concentrations
697 before the addition of Fe-spike at t=0h.

698



699

700 **Fig. 7** Distribution of PARAFAC components (A) C1, (B) C2, and (C) C3 along the salinity gradient and for

701 the different types of collected samples (*i.e.*, beach groundwater, massive ice, meltwater and nearshore

702 seawater samples). Note that there is only one massive ice sample reported here. For the boxplots, the black

703 lines represent the median values, the whiskers represent the extent of the data, and the dot points represent

704 the outlier values.

705

706

707